An investigation of partial cone cracks in silicon nitride balls

George Levesque *, Nagaraj K. Arakere

Department of Mechanical and Aerospace Engineering, University of Florida, P.O. Box 116300, Gainesville, FL 32611-6300, USA

ARTICLE INFO

ABSTRACT

Hybrid silicon nitride ball/steel raceway bearings are used in advanced aircraft engines and space propulsion systems. Silicon nitride is a brittle material and partial cone cracks, or c-cracks, originate from contact interactions during manufacturing. These cracks limit the Rolling Contact Fatigue (RCF) life of the balls. Here the authors examine subsurface Hertzian stresses between contacting spheres, using an analytical stress solution, to investigate their applicability to predicting and characterizing crack size and shape. The authors also incrementally develop these cracks through an iterative crack growth procedure using a 3D finite element analysis. Comparisons are then made to experimental images of the flaws in silicon nitride. By varying the initial conditions during the contact interaction of the balls we demonstrate that a wide range of cone and partial cone cracks, observed in practice, can be generated using both the analytical and numerical fracture mechanics approaches. Furthermore, an expression is presented for the impact velocity that induces a cone crack from a maximum radial stress criterion at the contact periphery.

© 2008 Elsevier Ltd. All rights reserved.

1. Introduction

Normal contact of spheres made of brittle materials has been analyzed extensively and is known to generate cone cracks (Chen et al., 1995; Lawn, 1994) (Fig. 1a). Normal indentation of a hard sphere into a brittle material typically results in a ring crack on the surface, which then propagates into a frustum of a cone. Auerbach (1891) and Hertz (1896) first investigated this problem in the 1890s and many have revisited the problem since. Lawn (1994) provides a comprehensive review of extensive investigations made subsequently, to elucidate a qualitative and quantitative description of the initiation and growth of cone cracks in brittle materials. Mackerle (2001) has provided a biography of indentation simulations and with an emphasis on ceramic materials (Mackerle, 2002). In contrast to these bodies of work, cracks generated by oblique contact have received much less attention.

Partial cone or c-cracks are the observed result of the oblique impact of brittle materials (Frank and Lawn, 1967) (Fig. 1b). These c-cracks are considered the most damaging surface defect that limits ball life in hybrid bearings under RCF (Evans, 1983; Hadfield et al., 1993a). c-Cracks are more commonly observed in sphere-to-sphere interactions and they not only have non-planar crack faces but also possess non-planar crack tips, as opposed to the axisymmetric cone cracks. This makes their shape more difficult to describe and, therefore, more difficult to analyze in any linear elastic fracture mechanics (LEFM) based analysis. Our goal is to obtain the possible range of crack shapes in three-dimensions that result from oblique interaction for future finite element (FE) analysis.

---

* Corresponding author. Tel.: +1 352 392 5425.
  E-mail address: gr8@ufl.edu (G. Levesque).

Nomenclature

a	contact patch radius
E	Young's modulus
E_1, E_2	Young's moduli for bodies 1 and 2, respectively
E^*	effective Young's modulus, $\left(\frac{1-v_1}{E_1} + \frac{1-v_2}{E_2}\right)^{-1}$
f	coefficient of friction
J	$\frac{xy}{3r^4}\left[\left(\frac{z}{u}\right)^3 - 3\left(\frac{z}{u}\right) + 2\right]$
m	effective mass, $\left(\frac{1}{m_1} + \frac{1}{m_2}\right)^{-1}$
N	a harmonic potential function (Love, 1927)
R	effective radius, $\left(\frac{1}{R_1} + \frac{1}{R_2}\right)^{-1}$
R_1, R_2	radius of sphere 1 and 2, respectively
r	radial cylindrical coordinate, $\sqrt{x^2 + y^2}$
p_0	max pressure
p_0^*	max pressure to induce cracking
T	a harmonic potential function (Love, 1927)
u	$\sqrt{\frac{1}{2}\left\{r^2 + z^2 - 1 + \sqrt{(r^2 + z^2 - 1)^2 + 4z^2}\right\}}$
u, v, w	displacements in x-, y-, and z-directions respectively
u_1, v_1, w_1	node 1 displacements in x-, y-, and z-directions, respectively
u_2, v_2, w_2	node 2 displacements in x-, y-, and z-directions, respectively
V	velocity of moving ball
V_z	velocity component of moving ball normal to the contact surface
μ	elastic potential
v	Poisson's ratio
v_1, v_2	Poisson's ratios for bodies 1 and 2 respectively
$\sigma_1, \sigma_2, \sigma_3$	first, second, and third principal stresses where $\sigma_1 \geqslant \sigma_2 \geqslant \sigma_3$
σ_c	contact periphery stress to induce cracking
$\sigma_{\max}$	contact periphery stress
$\sigma_{\max|f}$	contact periphery stress with friction
σ_{ij}^N	stress components from normal load
σ_{ij}^T	stress components from traction load
τ_{ij}^N	shear components of stress from normal load
τ_{ij}^T	shear components of stress from traction load

The analysis of crack shapes produced by oblique interactions has direct and immediate application. The performance of hybrid silicon nitride ball/steel raceway bearings has been shown to be much superior to steel bearings (Miner et al., 1996 and Tanimoto et al., 2000). However, silicon nitride balls are sensitive to surface defects and can fail from fatigue spalls emanating from pre-existing c-cracks, due to crack growth driven by RCF (Hadfield et al., 1993b). Silicon nitride (Si$_3$N$_4$) exhibits favorable material properties for application in hybrid high speed ball bearings such as high compressive strength, high hardness, a third of the density of steel, low coefficient of thermal expansion, and high corrosion and temperature resistance. However, it also has low fracture toughness (Piotrowski and O'Brien, 2006). Silicon nitride balls used in rolling-element bearings is an engineered ceramic product made from β phase Si$_3$N$_4$ needle-like crystals of approximately 2 μm grain size held by a glassy phase. Balls for aerospace applications are made by sintering and hot isostatic pressing of Si$_3$N$_4$ grains with the glassy phase forming roughly 1% of the volume fraction with ball diameter and surface finish held to submicron levels. The final ball dimension is achieved in a lapping process that produces (unavoidable) low velocity ball collisions resulting in surface cracks initiated by the radial tensile stress field at the contact periphery (Wang and Hadfield, 2000).

We present a qualitative and quantitative description of the range of possible partial cone crack shapes in 3D as functions of initial conditions (coefficient of friction and contact patch size) during oblique spherical contact. The emphasis is not on simulating the dynamics of oblique contacts, but simulating the interaction forces via the coefficient of friction and contact patch size, and then focusing on the effect of resulting subsurface Hertzian stress fields in inducing brittle fracture. The resulting 3D geometry of crack faces is predicted using the following two approaches: (1) an analytical description of 3D subsurface stress state is used to predict the crack front based on the max principal stress "trajectory" and (2) a 3D finite element contact stress analysis is used in conjunction with a numerical 3D fracture analysis program, FRANC3D, to grow the partial cone crack incrementally. Results from the two methods are compared and show good agreement. Qualitative features are examined from experimentally produced c-cracks in silicon nitride balls. By varying the initial conditions of the contact interaction we show that a wide range of partial cone cracks, observed in practice, can be generated using both
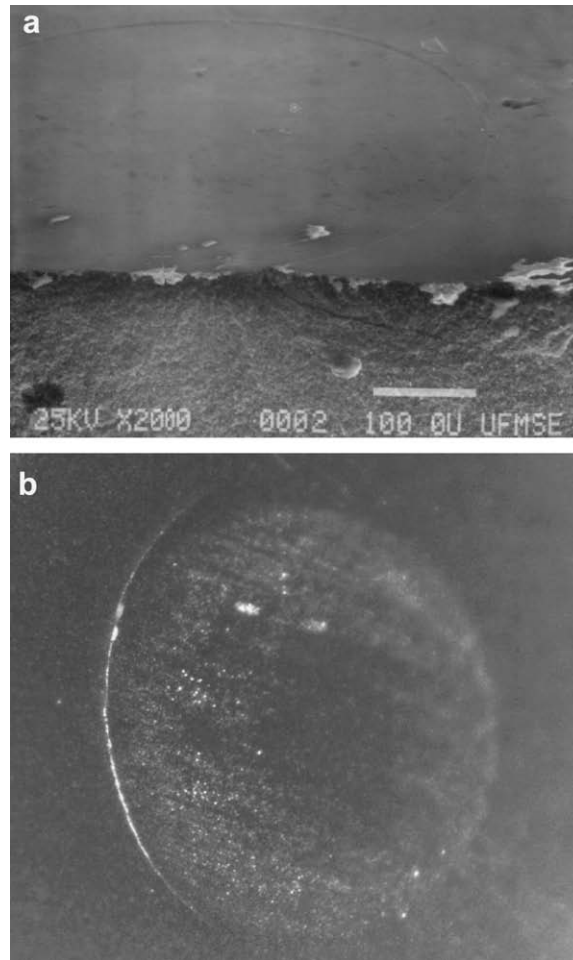
Fig. 1. (a) Example of a cone crack in silicon nitride (Mecholsky, 2008), (b) Experimental image of oblique sphere interaction with contact patch and resultant c-crack shown. Image in proportion but scales are not shown (Wolfe, 2008).

the analytical and numerical fracture mechanics approaches. The results generated are of immediate engineering relevance to the hybrid ball bearing industry towards evaluating critical flaw size for defining limits for non-destructive evaluation methods for silicon nitride ball quality control and for developing a fracture mechanics based life prediction methodology for hybrid bearings.

2. Analysis

Here we discuss the stress state and fracture mechanics approaches mentioned earlier to yield the range of partial cone crack shapes produced during oblique interaction. The stress-state analyses have been done for normal indentation for some time. The cone crack path due to a spherical indenter was shown by Frank and Lawn (1967), to a first approximation, to be orthogonal to the maximum tensile principal stress distribution of the statically loaded elastic half space. Later, Lawn (1967) showed that traction forces induced by a sliding spherical indenter strongly influenced the quasi-static stress field, and generated an early partial cone crack profile for brittle materials in two-dimensions. After the works of Frank and Lawn (1967), there was a continuing use of the max principal stress trajectory in cone crack analyses. As a result of this history, we will extend the stress-state analysis to describe the crack shapes in three-dimensions and discuss a couple variations.

Crack shape analysis has also been done using an incremental growth approach as endorsed by Kocer and Collins (1998). In later work on cone cracks, Kocer emphasizes that the study of stress in an uncracked body to determine a crack shape had not been analytically supported to be reminiscent of the resultant crack shape (as once a crack exists, the stress field changes significantly and the crack grows in compliance with this new stress field) and so believed that the crack shape should be acquired based upon an iterative crack growth analysis (or an experimental approach). We conduct an incremental crack growth analysis, and in the case of the partial cone cracks, an iterative crack growth study can only be done correctly in

three-dimensions. Doing such a fracture mechanics analysis using 3D FEA requires the ability to incrementally grow cracks and remesh, resulting in a computationally intensive endeavor.

We will compare these two analyses with experimental images that we have obtained through multiple sources. The surface dimension of c-cracks typically seen in Si_3N_4 balls ranges from 50–400 μm, depending on the ball diameter (Wang and Hadfield, 2000). Experimental examination of crack shape of these very small cracks that are embedded in a non-translucent material like Si_3N_4 which is difficult to cut or grind, and hence poses considerable difficulty.

2.1. Stress-state analysis

To attempt to generate the crack shape from its uncracked stress state, we must first obtain the stress state of obliquely interacting spheres. Oblique impact with contact friction gives rise to tangential tractions potentially leading to micro-slip at the interface. The complex interaction between tangential traction and micro-slip and their time-history dependence has been visited by Mindlin and Deresiewicz (1953) and analyzed by Maw et al. (1976, 1981). However, these surface tractions are not closed-form and more difficult to incorporate into a 3D subsurface stress-field solution and are not worth the possible loss in accuracy (Andersson, 1996). Also, balls are typically well lubricated during the lapping process where these cracks originate. With this support, we conduct a sliding contact analysis.

To investigate cone and c-crack size and shape as a function of normal and traction force distributions, we use a comprehensive 3D analytical subsurface stress solution for efficiency. The Hertz theory of quasi-static impact holds for evaluating the variation of contact size and contact pressure during impact under familiar criteria of ball velocities relative to wave speeds (Johnson, 1987). Applying superposition for normal and tangential stresses, the Hertz normal pressure is given by

$$p(r) = -p_0\sqrt{1 - r^2} \tag{1}$$

where p_0 is the peak pressure and r is the cylindrical coordinate. For a contact in full slip, the tangential traction distribution is $f * p(r)$, where f is the coefficient of friction, and this distribution is used throughout our simulations.

Hamilton and Goodman (1966) presented the 3D subsurface stress distribution for a spherical sliding contact. The Cartesian coordinate system is used in the configuration displayed in Fig. 2. To acquire a solution, the harmonic potentials, N and T, are chosen to satisfy the necessary boundary conditions, namely:
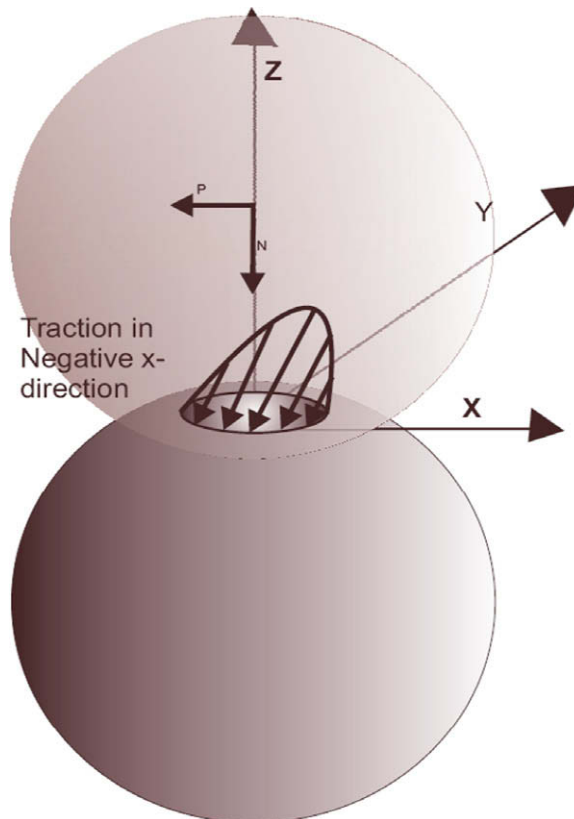

Fig. 2. Diagram of coordinate system for the equations of stress for oblique colliding spheres where N and P denote the normal and perpendicular load components.

$$\sigma_{zz} = \frac{\tau_{zx}}{f} = p(r) \quad r \leqslant a \tag{2a}$$

$$\sigma_{zz} = \tau_{zx} = 0 \quad r > a \tag{2b}$$

So they may be substituted into the relations for displacements u, v, and w, (Love, 1927) namely:

$$2\mu u = -(1 - 2v)N_{,x} - zN_{,xz} + 2vT_{,xx} + 2T_{,zz} - zT_{,xxz} \tag{3a}$$

$$2\mu v = -(1 - 2v)N_{,y} - zN_{,yz} + 2vT_{,xy} - zT_{,xyz} \tag{3b}$$

$$2\mu w = 2(1 - v)N_{,z} - zN_{,zz} + (1 - 2v)T_{,zx} - zT_{,xzz} \tag{3c}$$

where commas denote derivatives and v is the Poisson's ratio.

Solutions are given elsewhere (Hamilton, 1983; Sackfield and Hills, 1983 and Hills et al., 1992) and are reproduced below for completeness.

$$\frac{\sigma_{xx}^N}{p_0} = (1 - 2v)\frac{1}{3r^4}(x^2 - y^2)\left(1 - \frac{z^3}{u^3}\right)$$
$$+ \frac{z}{u}\left[(1 + v)u\arctan\left(\frac{1}{u}\right) - 2v - (1 - v)\frac{u^3}{1 + u^2} - (1 - 2v)\frac{x^2}{r^2(1 + u^2)} - \frac{x^2 u^4}{(1 + u^2)^2(u^4 + z^2)}\right] \tag{4a}$$

$$\frac{\sigma_{yy}^N}{p_0} = (1 - 2v)\frac{1}{3r^4}(x^2 - y^2)\left(\frac{z^3}{u^3} - 1\right)$$
$$+ \frac{z}{u}\left[(1 + v)u\arctan\left(\frac{1}{u}\right) - 2v - (1 - v)\frac{u^2}{1 + u^2} - (1 - 2v)\frac{y^2}{r^2(1 + u^2)} - \frac{y^2 u^4}{(1 + u^2)^2(u^4 + z^2)}\right] \tag{4b}$$

$$\frac{\tau_{xy}^N}{p_0} = \frac{-xyzu^3}{(1 + u^2)^2(u^4 + z^2)} + (1 - 2v)J \tag{4c}$$

$$\frac{\sigma_{zz}^N}{p_0} = \frac{-z^3}{u(u^4 + z^2)} \tag{4d}$$

$$\frac{\tau_{zx}^N}{p_0} = \frac{-xz^2 u}{(1 + u^2)(u^4 + z^2)} \tag{4e}$$

$$\frac{\tau_{yz}^N}{p_0} = \frac{-yz^2 u}{(1 + u^2)(u^4 + z^2)} \tag{4f}$$

$$\frac{\sigma_{xx}^T}{fp_0} = -\left[\frac{\sigma_{yy}^T}{fp_0} + \frac{\sigma_{zz}^T}{fp_0}\right] - x(1 + v)\left[\arctan\left(\frac{1}{u}\right) - \frac{u}{(1 + u^2)}\right] \tag{4g}$$

$$\frac{\sigma_{yy}^T}{fp_0} = 2vx\left[-\frac{3}{8}\arctan\left(\frac{1}{u}\right) + \frac{u}{4(1 + u^2)^2} + \frac{3u}{8(1 + u^2)} - \frac{y^2 u^5}{(1 + u^2)^3(u^4 + z^2)}\right] + (1 - 2v)z\frac{\partial J}{\partial y} \tag{4h}$$

$$\frac{\sigma_{zz}^T}{fp_0} = -\frac{xz^2 u}{(1 + u^2)(u^4 + z^2)} \tag{4i}$$

$$\frac{\tau_{yz}^T}{fp_0} = -\frac{xyzu^3}{(1 + u^2)^2(u^4 + z^2)} \tag{4j}$$

$$\frac{\tau_{zx}^T}{fp_0} = z\left[\frac{3}{2}\arctan\left(\frac{1}{u}\right) - \frac{1}{u} - \frac{u}{2(1 + u^2)} - \frac{x^2 u^3}{(1 + u^2)^2(u^4 + z^2)}\right] \tag{4k}$$

$$\frac{\tau_{xy}^T}{fp_0} = 2vy\left[\frac{1}{8}\arctan\left(\frac{1}{u}\right) - \frac{u}{8(1 + u^2)} + \frac{u}{4(1 + u^2)^2} - \frac{x^2 u^5}{(1 + u^2)^3(u^4 + z^2)}\right] - \frac{y}{2}\left[\arctan\left(\frac{1}{u}\right) - \frac{u}{1 + u^2}\right] + (1 - 2v)z\frac{\partial J}{\partial x} \tag{4l}$$

where

$$J = \frac{xy}{3r^4}\left[\left(\frac{z}{u}\right)^3 - 3\left(\frac{z}{u}\right) + 2\right] \tag{5}$$

and

$$u^2 = \frac{1}{2}\{r^2 + z^2 - 1 + \sqrt{(r^2 + z^2 - 1)^2 + 4z^2}\} \qquad (6)$$

The formulation used here, for spheres in sliding contact, is nondimensionalized such that the only inputs required are a Poisson's ratio (v), coefficient of friction (f), and magnitude of p_0. The stress has been normalized with respect to (w.r.t.) p_0 and the contact patch is normalized w.r.t. itself and always is at $r = 1$. Fig. 3 is an example contour plot. At points close to the surface, coordinate planes and axes, and at $r = 1$, the limits of these functions were evaluated for efficiency and to avoid numerical difficulties.

With a 3D stress field well described, we move to generate the shape of the c-cracks according to the max principal stress trajectory for brittle materials by Frank and Lawn (1967). When max principal stress "trajectory" was used by Frank and Lawn, they left the phrase largely undefined. Generally, "trajectory" refers to some curve that intersects a family of surfaces at the same angle. However, for any given angle (say 90°) there are an infinite number of surfaces that can cut through the contours of max principal stress values. We can see they implied to generate a line that cut through the contours at 90° and originated at the surface, near the edge of the contact patch, and thus followed something close to the direction of maximum change in the field. Doing so computationally in a 3D field can quickly become difficult as gradients of stress become demanding depending on the level of refinement necessary (especially near the surface) (no matter if the stress state is being evaluated using equations or the finite element method). Also, as the point of crack origin is not always in agreement to what is seen in experiment (Kocer and Collins, 1998) some perturbations about the contact periphery are necessary to see the changes in crack shape for a given stress field.

A trajectory approach, like Frank and Lawn (1967) was extended to three dimensions, where we plot the 3D contours of the third (minimum) principal stress according to $\sigma_3(1 + \varepsilon, 0, 0) = \sigma_3(x, y, z)$ where ε is a chosen small value that forces the contour value of interest to be near the periphery of the contact. This method functions well because it is orthonormal at the intersections of contours of the max principal stress and has a similar result to searching out the direction of max change in the max principal stress. However, it should be noted that the choice of epsilon is significant since the stresses on the periphery of the contact is quite rapid and two close adjacent contours will diverge from each other as distance from the contact periphery increases. The cracks displayed in Fig. 4 are examples of this procedure. The method is effective in generating cone cracks for normal contact and partial cone cracks for oblique contact. The generated cone angle of 63° to the vertical agrees with experimental observations (Kocer and Collins, 1998).

Briefly, we also generated similar crack shapes using two other techniques. For example, a maximum tensile stress approach, where we search the 3D stress field for points which are maxima in the z direction according to $\frac{\partial \sigma_1(x,y,z)}{\partial z} = 0$ and these points are then connected to form smooth, continuous plane originating at the contact periphery. Also, a plane of maximum change where we have investigated the surfaces produced by local maxima. [When investigating local maxima we are forced to choose a coordinate variable in which the max principal stress undergo maximum change. Here we note that we find the surfaces produced by $\frac{\partial \sigma_1}{\partial r} = 0$ (for cone cracks) and $\frac{\partial \sigma_1}{\partial x} = 0$ (for c-cracks) agree best with experimental observation.] These two methods were seen to be similar when the derivatives were taken with respect to the mentioned variables.
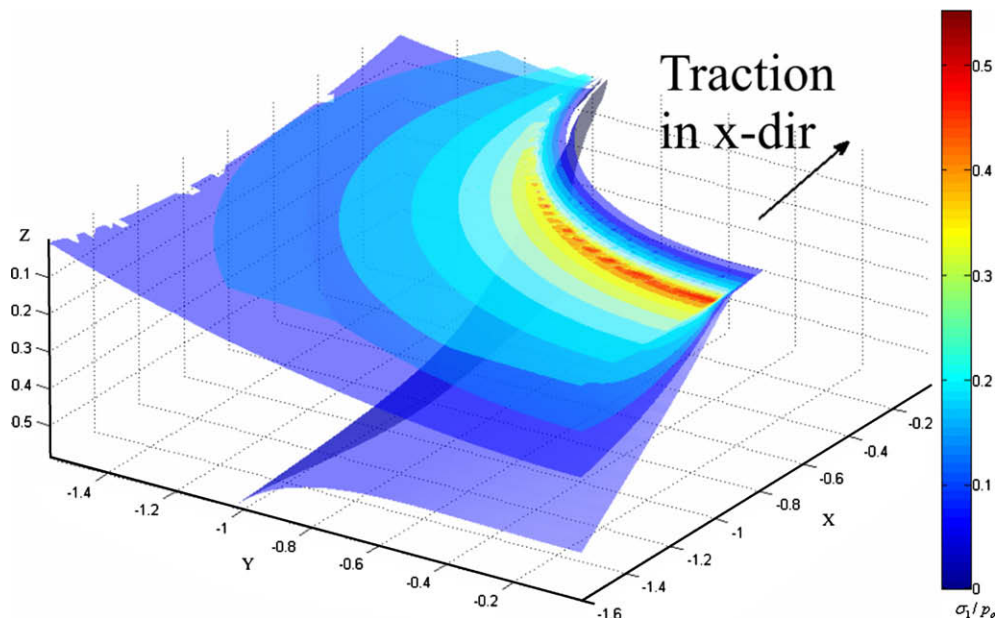

Fig. 3. Surfaces representing constant values of the max principle stress field nondimensionalized with respect to the applied pressure (σ_1/p_0).
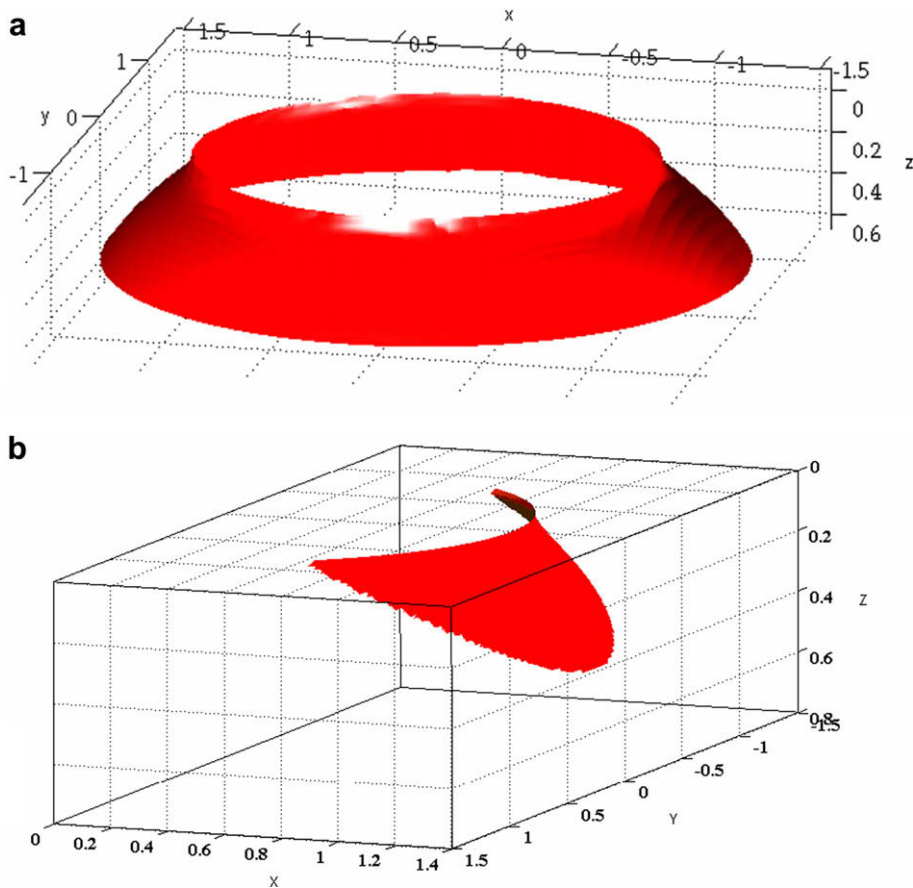
Fig. 4. (a) The cone crack as generated from the Hertzian stresses without traction. (b) A c-crack generated for $v = 0.3$ and $f = 0.1$.

Since the contact patch radius has been normalized w.r.t. itself, the crack shapes generated are attributable to all cracks that are generated by contacting spheres with the prescribed Poisson's ratio (which produces little effect when analyzing the parametric variation) and coefficient of friction but its size must be scaled to the crack-generating contact patch. The generated crack surface is smoothed by a moving average on a discrete number of evaluation points [by the smooth( ) function in Matlab (Mathworks, 2005)] and then patched for a 3D plane [by the patch( ) function (Mathworks, 2005)]. Since the surfaces produced by the above procedure are based on stress distributions alone, they can differ from the physical cracks whose extension is limited by the physics of dynamic brittle fracture. We will explore a stress-analysis based criterion to determine the crack depth in a subsequent paper. For this work, surfaces were curtailed to show common cracking proportions observed through experiments.

2.2. Incremental crack growth analysis

The authors also generated the 3D partial cone crack using the finite element method and an incremental crack growth procedure to compare with the stress-state results. Starting with an initial small penny shaped crack, the crack was then incrementally grown using the crack growth software FRANC3D/NG developed by the Fracture Analysis Consultants (2005) after being analyzed by the commercial finite element software ABAQUS (Desault Systemes, 2007). Earlier versions of FRANC2D and FRANC3D, based on work by Swensona and Ingraffea (1987, 1988a,b), were primarily used for isotropic materials. The current version of FRANC3D/NG FEA based fracture analysis program can analyze cracks in anisotropic materials and is based on Banks-Sills et al. (2005, 2007). With an adaptive mesh technique, this fracture software can simulate crack growth without prescribing the crack path. Their work has provided fundamental understandings for the simulation of crack propagation based on FEA. In this analysis, FRANC3D/NG was used to mesh a crack, analyze the FEM calculated displacements in ABAQUS (Desault Systemes, 2007) to determine stress intensity factors, determine crack turning angles, and extend and mesh the crack. Silicon nitride is treated as an isotropic material in this analysis. While FRANC3D/NG is normally used for fatigue crack growth, we will use its abilities to incrementally grow and remesh cracks to simulate c-crack creation.
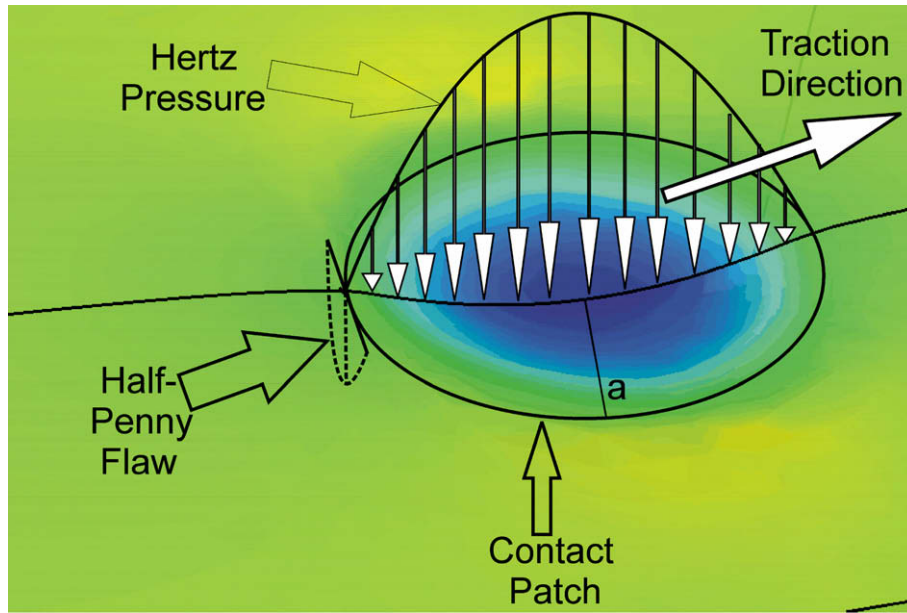
Fig. 5. Initial configuration of crack and load at the beginning of the crack growth analysis in the FE model.

In 3D FEA, a small vertical half-penny flaw (a = 10 μm b = 10 μm) was inserted into a silicon nitride block (E = 310 GPa, v = 0.28). The body was meshed with a combination of quadratic hexahedral, pyramidal, and tetrahedral elements (so that the crack had collapsed hexahedral quarter point elements to preserve the singularity and avoid warning elements), which totaled around 25,000 elements. In the vicinity of the crack, the size of the elements was about 1/40th of the crack width in order to have sufficient mesh density for the applied load. This part was loaded according to Fig. 5 with an applied Hertz pressure distribution, as analyzed with the stress analysis technique and is fixed far-field. Far-field boundary conditions were simulated on this small cracked block using a submodeling technique (Desault Systemes, 2007) where displacements are interpolated from a larger block undergoing the same load orientation and is fixed at its furthest side. To grow a crack after the displaced state is calculated, stress intensity factors for isotropic materials are calculated by the displacement correlation equations:

$$K_I = \frac{E}{4(1-v^2)}\sqrt{\frac{2\pi}{r}}(u_1 - u_2) \tag{7a}$$

$$K_{II} = \frac{E}{4(1-v^2)}\sqrt{\frac{2\pi}{r}}(v_1 - v_2) \tag{7b}$$

$$K_{III} = \frac{E}{4(1-v^2)}\sqrt{\frac{2\pi}{r}}(w_1 - w_2) \tag{7c}$$

The computed stress intensity factors are inserted into the maximum tensile stress crack turning angle criteria (Erdogan and Sih, 1963) and then the crack is extended an average length as specified by the user according to a relative extension power law written as:

$$\Delta a_{nodei} = \Delta a_{mean}\left(\frac{\Delta K_{nodei}}{\Delta K_{mean}}\right)^n \tag{8}$$

where the exponent, n, is iteratively chosen to avoid high gradients in the stress intensity factors along the crack front and the average length, Δa_{mean}, was often chosen to be about 10 μm. Incremental remeshing was stopped once we reached the relative proportions of cracks observed in experiment. Images of incremental growth are shown for f = 0.1 and f = 0.5 in Fig. 6 and for f = 0.5 in Fig. 7.

3. Results and discussion

Three-dimensional crack shapes resulting from the stress-state analysis exhibit the following characteristics: (a) the shape of the cone crack is expectedly axisymmetric and exhibits the experimentally observed angle of approximately 63° to the vertical (Frank and Lawn, 1967) and (b) when spheres collide obliquely the resulting max tensile stress is in the wake of the contact and is the site of c-crack origination. From the stress-state examination, we
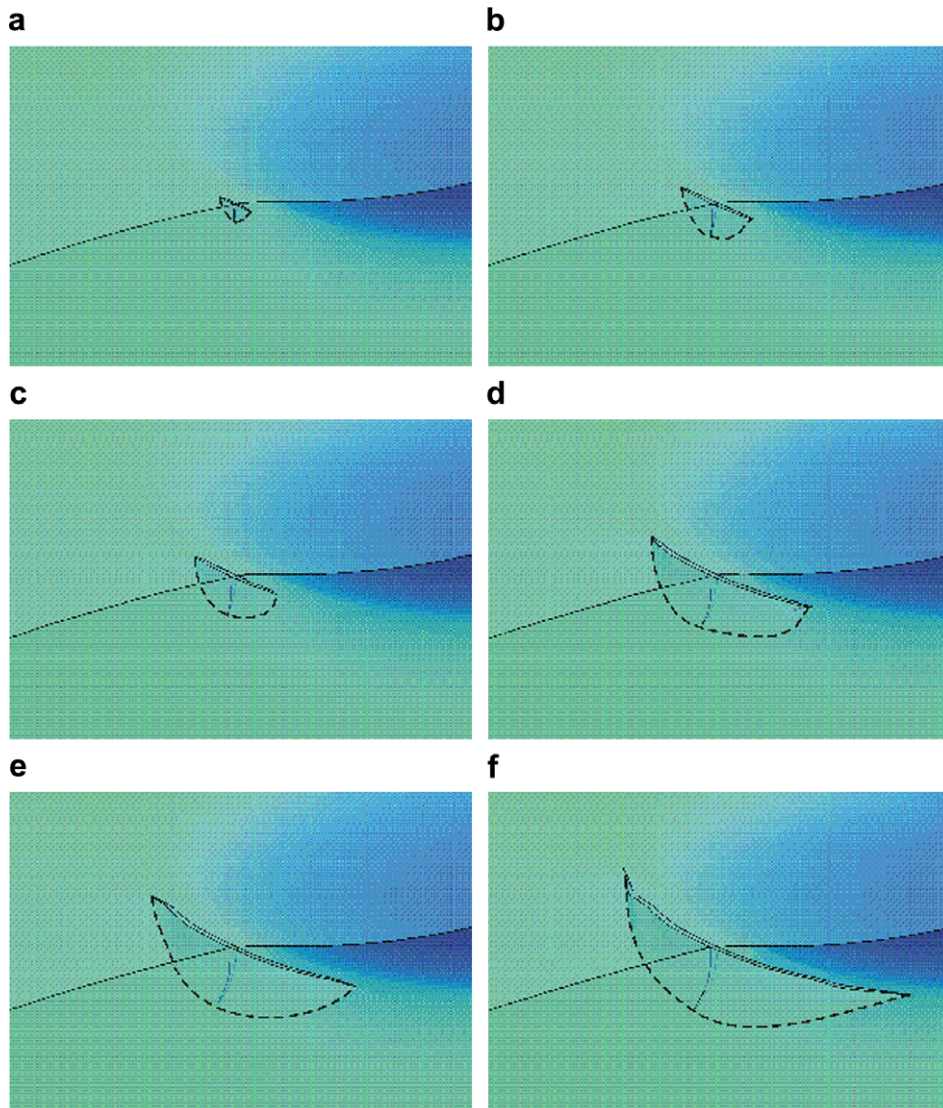
Fig. 6. Incremental images of crack growth for f = 0.1. (a) half-width = 0.04 a, depth = 0.07 a, (b) half-width = 0.07 a, depth = 0.14 a, (c) half-width = 0.09 a, depth = 0.16 a, (d) half-width = 0.11 a, depth = 0.32 a, (e) half-width = 0.12 a, depth = 0.41 a, (f) half-width = 0.15 a, depth = 0.58 a.

observe that a c-crack is unlikely to circumvent more than 180° about the contact patch since the other side of the contact region is in compression. Research on silicon nitride confirms that their circumference is between a third and a fourth of a complete circle (Hadfield et al., 1993b). Also, c-cracks tend to depart from the contact patch radii as friction increases (see Fig. 1b). Furthermore, a plot of the c-cracks produced as a result of different friction coefficients (Fig. 8) shows that the range of c-crack angles observed (Zhao et al., 2006) are accounted for and that higher coefficients of friction increase the radius of the c-crack on the surface and steeper cracks. The results are summarized in Table 1.

We compare cross-sectional images produced by our methods to those examined in experiment. Firstly, we show and array of cracks from Zhao et al. (2006) which is a collection of "naturally" occurring (those which result from the manufacturing process) c-cracks in Si_3N_4 with a range in steepness (Fig. 9). We also display images of artificially produced cracks (created in laboratory settings on finished balls) in Fig. 10 (Wolfe, 2008).

Reflecting on our incremental growth results we see that the range of crack shapes produced by the two analyses are quite similar and agree with the range of shapes that we observe in experiment. The incremental growth analysis may produce small perturbations from the actual crack shape that can expectedly result from an incremental remeshing technique. The incremental growth analysis also tends to have more curvature as it extends into the material as opposed to the stress state analysis. Also, the incremental results seem to conform to the contact patch more than the stress results that may be the result of the incremental approach. A superposed image of the incrementally grown crack was developed by importing
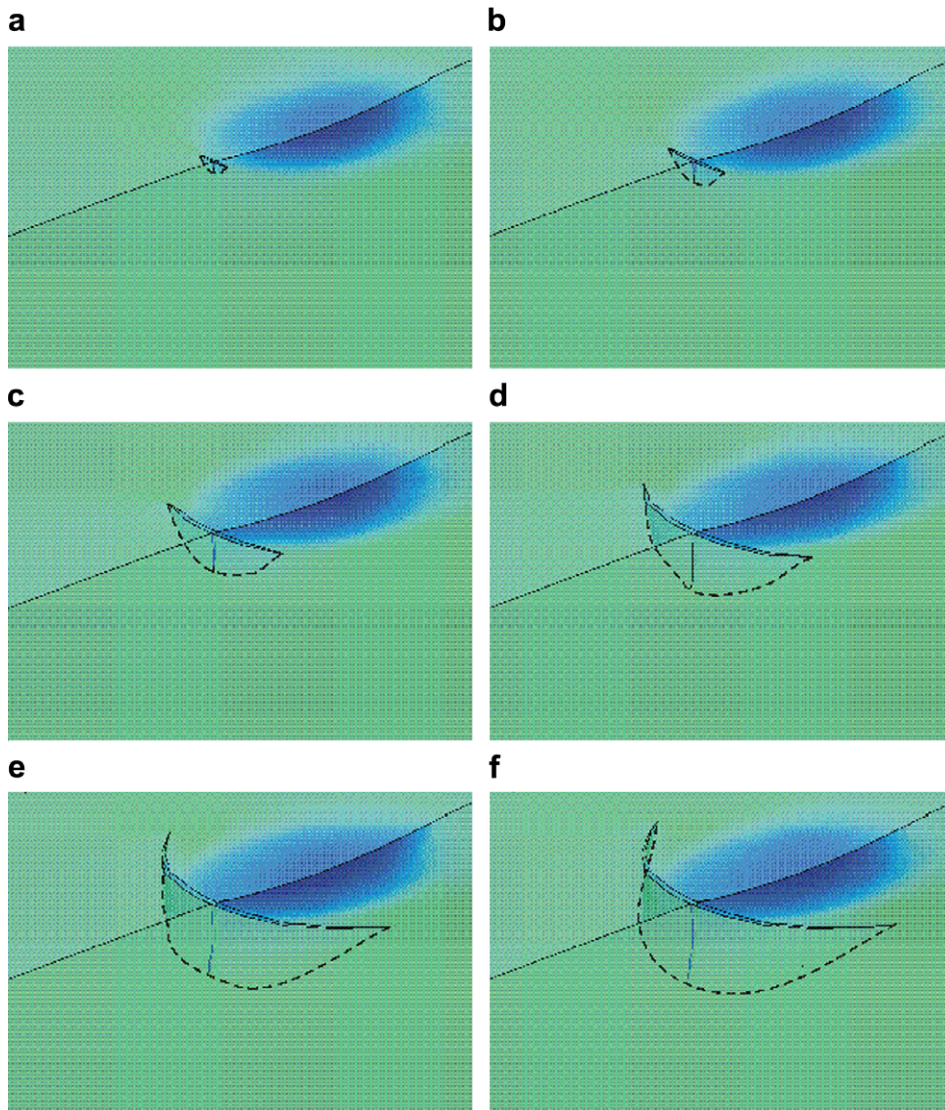
Fig. 7. Incremental images of crack growth for f=0.5. (a) half-width = 0.11 a, depth = 0.17 a, (b) half-width = 0.17 a, depth = 0.35 a, (c) half-width = 0.29 a, depth = 0.69 a, (d) half-width = 0.39 a, depth = 1.07 a, (e) half-width = 0.523 a, depth = 1.46 a, (f) half-width = 0.59 a, depth = 1.59 a.

the global coordinates of the created crack into Matlab and performing Delaunay triangulation (Mathworks, 2005) to obtain a series of triangles that were plotted as a triangular surface plot. The result is reminiscent of the actual mesh (see Fig. 11). Comparing the two shapes, they are in excellent agreement on the midsection where increments were comparably smaller but were somewhat divergent on the surface.

As a result, we can see the benefits of both approaches. The incremental crack growth analysis is well supported by a history of LEFM-based analysis but regions of significant crack turning may take significant amounts of computational effort as the size of the Δa_{mean} must be decreased. The incremental growth analysis also produces a meshed part that the user can apply under any other type of loading for other analyses. The stress-state analysis is relatively fast to implement and runs without user interaction. In addition, their good agreement may leave both as viable options for future analysts depending on the analyst's time and needs.

With this family of crack shapes, one conducting an analysis on these types of cracks should consider the range of steepness and proportion produced by our analysis. Since the range of crack shapes produced is observed in experiment, we feel that an examination of the uncracked stress field can yield accurate predictions of crack shapes for brittle materials and propose the method to be used in other instances where a stress field is known (even by computational methods) and the stress field is torsion free (Frank and Lawn, 1967) as long as the researchers note the possible variation of traction in the (small) contact region. Also, these results are in excellent agreement with the shapes produced by an iterative remeshing technique
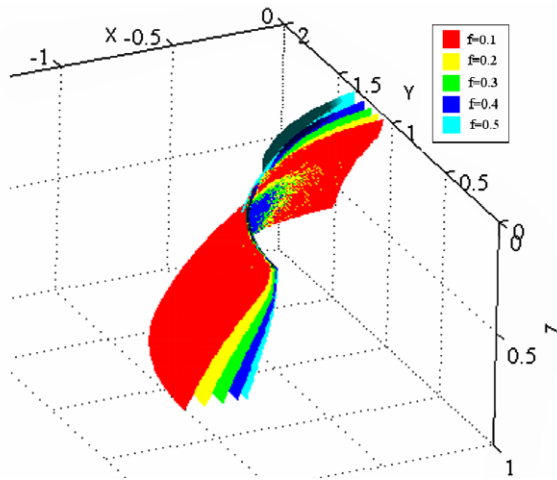
Fig. 8. Cracks produced in our coordinate system for f = 0.1, 0.2, 0.3, 0.4, 0.5, and v = 0.28. Note the increasing surface radius and steepness with the increase of the friction coefficient.

Table 1
Crack radius on the surface (nondimensionalized w.r.t. the contact patch) and an estimate of angle in degrees measured down from the surface for c-cracks produced by different values of f from stress-state analysis

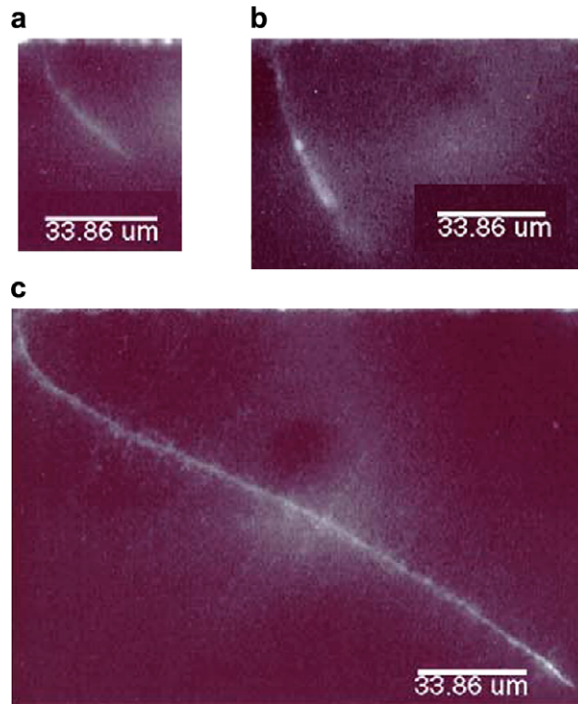| f	Crack radius	Angle to ball surface
0.1	1.07	48
0.2	1.12	54
0.3	1.17	63
0.4	1.22	72
0.5	1.28	77

Fig. 9. Cross-sections of multiple "natural" c-cracks on 12.7 mm diameter, grade 5 balls that (after manufacturing) had a typical 0.01 μm roughness. See Zhao et al. (2006) for details.
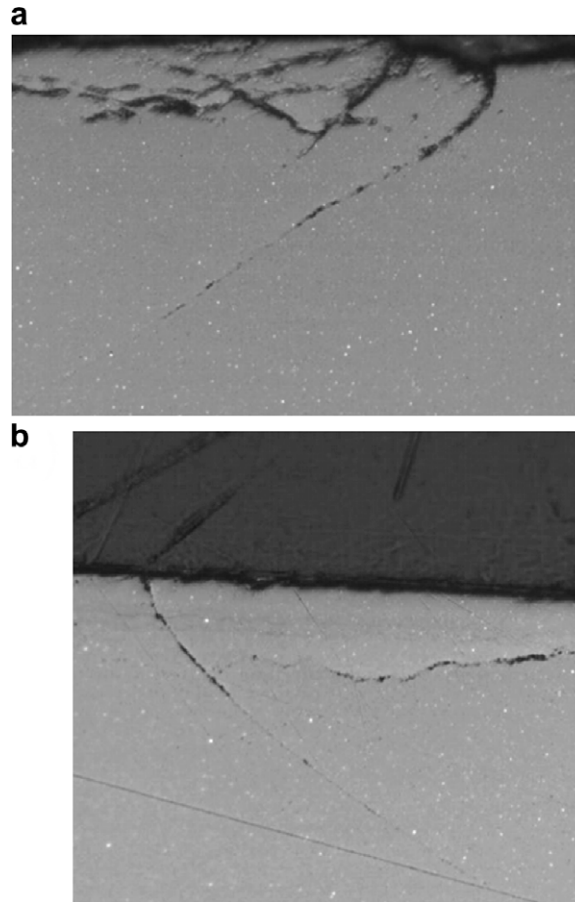
a

b

Fig. 10. Cross-sections of artificially produced c-cracks. Images in proportion but scales are not shown. Images courtesy of Timken (Wolfe, 2008).

that requires the user to have an adequate mesh and a small increment of crack advance. As an added benefit, the iterative analysis creates a mesh suitable for analysis of c-cracks under RCF.

4. Practical observations

Our analysis shows that the crack nucleates and grows from the point in the trailing contact periphery of the oblique interaction, as that is where stress is at a maximum. With this knowledge, we can reflect upon the contact of spheres and develop predictive equations concerning crack nucleation.

There have been a few studies that have normally loaded silicon nitride spheres until cracking was detected by acoustic emission (Ichikawa et al., 1995a,b; and Ohgushi and Ichikawa, 1996). Interestingly, they have found a range of the maximum Hertz contact pressure to induce cracking to be in the range of 14-18 GPa. With this number we can approximate the velocity to impart collisions for normal interactions. We recall that the maximum principal stress from a normal spherical contact on the surface contact periphery is

$$\sigma_{\max} = \sigma_{rr} = \frac{1-2v}{3}p_0 \tag{9}$$

Which, for a Poisson's ratio of 0.28, the normal contact equation yields,

$$p_0 \approx 6.8\sigma_{\max} \tag{10}$$

If we substitute 16 GPa as the max pressure (the median of those pressures that have been observed to cause cracking) we find a maximum periphery stress of 2.3 GPa. To find the normal velocity to induce this stress (without the influence of traction) we can use

$$p_0^* = \frac{3}{2\pi}\left(\frac{4E^*}{3R^{\frac{3}{4}}}\right)^{\frac{4}{5}}\left(\frac{5mV_z^2}{4}\right)^{\frac{1}{5}} \tag{11}$$

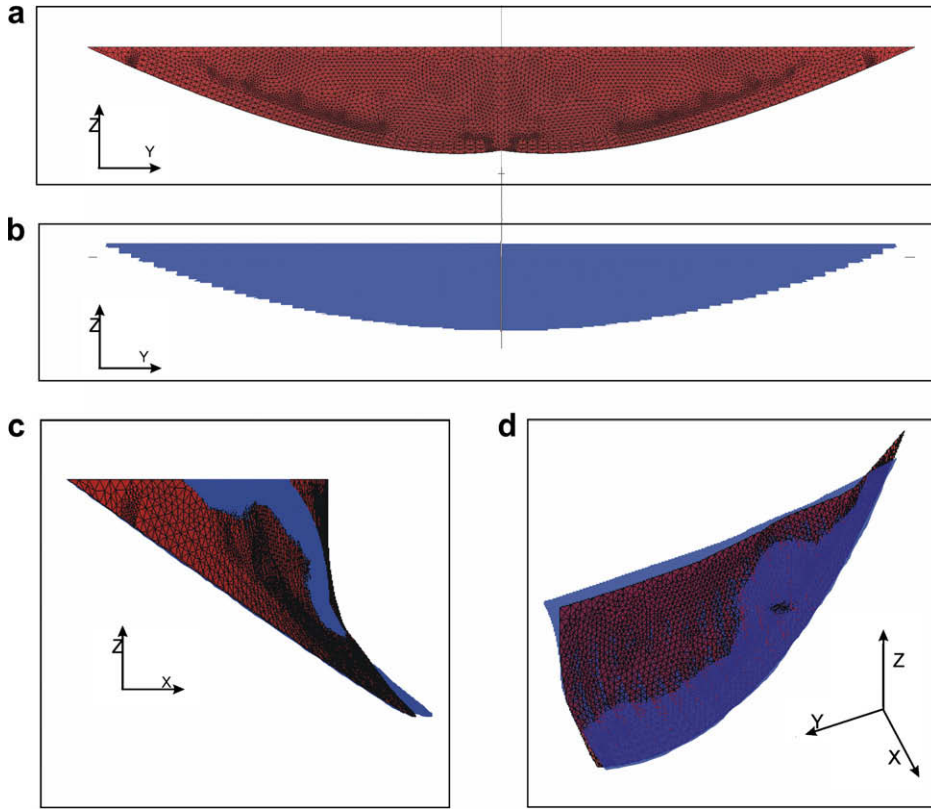(Johnson, 1987) and substitute Eq. 10 for p_0 to get:

Fig. 11. For f = 0.1, we show from the front (a) incremental growth crack, (b) stress-state crack. Superposed images of half-cracks produced by the stress-state (in blue) and the incremental growth (in red) at (c) the cracks midsection and d) from an azumuthal angle of 45° and a elevation angle of 18° as defined by matlab (Mathworks, 2005).

$$V_z = \frac{51\sqrt{5}}{50} \frac{\sigma_c^{\frac{5}{2}} R^{\frac{3}{2}} m^{\frac{1}{2}}}{E^{*2}} \tag{12}$$

Substituting, for a normal collision of silicon nitride bodies with a density of 2600 kg/m³ and radius of 6.35 mm (half inch diameter), we get a velocity of only 16 cm/s, which would need to be verified by experiment. It is not surprising then that surface cracks are generated during low velocity collisions generated during the ball lapping operation. The impact velocity required to cause subsurface yielding during collision between a hard steel ball and a medium hard steel ball with an yield strength of 1 GPa is 14 cm/sec (Johnson, 1987), and for balls made of brittle material exhibiting minimal yielding such as Si_3N_4 the impact energy is absorbed in the fracture surface generation.

We also note that the maximum periphery stress may be derived for sliding friction for use in maximum contact periphery stress criteria. First we take the limits of Eqs. 4a–4l as z and y approach 0 and x approaches 1 and then use the resulting components in the stress matrix to find the equation that represents the maximum root of the eigenvalue problem. The result is

$$\sigma_1(1,0,0) = \sigma_{\max|f} = p_0 \left[\frac{1-2v}{3} + f \frac{\pi}{2} \left(1 + \frac{v}{4} \right) \right] \tag{13}$$

which is expectedly a function of the contact pressure, the Poisson's ratio, and the friction coefficient. Comparing Eq. (13) with Eq. (9) we note that the p_0 required to induce cracking is reduced with a nonzero friction coefficient.

We can make another approximation from these results concerning crack nucleation. Taking the periphery stress to initiate cracking, 2.3 GPa, and the fracture toughness of 6 MPa$\sqrt{\text{m}}$, (Piotrowski and O'Brien, 2006) we can calculate, using $K = \sigma\sqrt{\pi a}$, an initial flaw size of .21 μm (roughly 2/5th of the grain size) from which these larger cracks could nucleate.

5. Conclusions

Our analysis of oblique contacting spheres lead to the following conclusions:

(1) Three approaches are presented that operate on the 3D subsurface stress field and effectively predict potential crack shapes for both the axisymmetric cone crack and the oblique resultant c-crack for Hertzian fracture.

(2) An iterative, three-dimensional crack growth simulation can also be used to generate the potential crack shapes.

(3) We found both methods to agree well with each other and experimental images.

(4) The methods can predict a wide range of crack shapes observed in oblique interactions by varying the friction coefficient at the contact.

(5) With knowledge derived from this investigation, we could approximate a maximum periphery stress to induce cracking, an equation to determine the velocity required to induce cracking, and an approximation of the original flaw size from which cracks may nucleate.

(6) An equation was derived for calculation of the maximum tensile periphery stress that drives crack nucleation, including the effect of friction.

While we have not originally intended for these analyses to be deterministic of crack shapes from the initial conditions of colliding spheres, our results have indicated the expected range of crack shapes in three separate ways: experimental reflection, a stress-state analysis and an iterative growth technique.

Acknowledgement

References

Andersson, M., 1996. Stress distribution and crack initiation for an elastic contact including friction. Int. J. Solids Struct. 33, 3673–3696.

Auerbach, F., 1891. Absolute hardness. Ann. Phys. Chem. 43, 61–100.

Banks-Sills, L., Hershkovitz, I., Wawrzynek, P.A., Eliasl, R., Ingraffea, A.R., 2005. Methods for calculating stress intensity factors in anisotropic materials. Part I: −z = 0 is a symmetry plane. Eng. Fract. Mech. 72, 2328–2358.

Banks-Sills, L., Wawrzynek, P.A., Carter, B., Ingraffea, A.R., Hershkovitz, I., 2007. Methods for calculating stress intensity factors in anisotropic materials. Part II: Arbitrary geometry. Eng. Fract. Mech. 74, 1293–1307.

Chen, S.Y., Farris, T.N., Chandrasekar, S., 1995. Contact mechanics of Hertzian cone cracking. IJSS 32, 329–340.

Desault Systemes, 2007. ABAQUS Theory Manual, Dessault Systémes, Providence, RI.

Evans, A.G., 1983. In: Riley, P.L. (Ed.), Progress in Nitrogen Ceramics. Martinus Nijhoff Publishers, The Netherlands, p. 595.

Erdogan, F., Sih, G.C., 1963. On the extension of plates under plane loading and transverse shear. J. Basic Eng. 85, 519–527.

Fracture Analysis Consultants, , Ithica, NY, 2005. Available from: <www.fracanalysis.com>.

Frank, F.C., Lawn, B.R., 1967. On the theory of Hertzian fracture. Proc. Roy. Soc. Lond. Ser. A 299, 291–306.

Hamilton, G.M., Goodman, L.E., 1966. The stress field created by a circular sliding contact. J. Appl. Mech. 33, 371.

Hamilton, G.M., 1983. Explicit equations for the stresses beneath a spherical sliding contact. Proc. Inst. Mech. Eng. 217 (2), 281.

Hadfield, M., Stolarski, T.A., Cundhill, R.T., Horton, 1993a. Failure modes of ceramics in rolling contact. S. Proc. Roy. Soc. Lond. Ser. A 443, 607–621.

Hadfield, M., Stolarski, T., Cundill, R.T., Horton, S., 1993b. Failure modes of ceramic elements with ring crack defects. Tribol. Int. 26, 157–164.

Hertz, H., 1896. Hertz's Miscellaneous Papers. McMillan, London.

Hills, D.A., Nowell, D., Sackfield, A., 1992. Mechanics of Elastic Contacts. Butterworth-Heinemann, Oxford. pp. 203–208.

Ichikawa, M., Takamatsu, T., Shindou, N., Okabe, N., Abe, Y., 1995a. Ring crack initiation load of silicon nitride bearing balls. JSME Int. J. Ser. A Mech. Mat. Eng. 38 (2), 226–230.

Ichikawa, M., Takamatsu, T., Matsuo, T., Okabe, N., Abe, Y., 1995b. Intra-ball and inter-ball variability of ring crack initiation load of silicon nitride bearing balls. JSME Int. J. Ser. A Mech. Mat. Eng. 38 (2), 231–235.

Johnson, K.L., 1987. Contact Mechanics. Cambridge Press, Cambridge. pp. 355–361.

Kocer, C., Collins, R.E., 1998. Angle of Hertzian cone cracks. J. Am. Ceramic Soc. 81 (7), 1736–1742.

Lawn, B.R., 1994. Indentation of ceramics with spheres: a century after Hertz. J. Am. Ceramic Soc. 81, 1794–1977.

Lawn, B.R., 1967. Partial cone crack formation in a brittle material loaded with a sliding spherical indenter. Proc. Roy. Soc. 299, 307.

Love, A.E.H., 1927. Treatise on the mathematical theory of elasticity. Dover Publications, NewYork.

Mathworks, Inc., 2005. MATLAB Function Reference Manual, Version 7.0.4.365 (R14) Mathworks, Inc., Cambridge, MA.

Mackerle, J., 2001. Finite element and boundary element analysis on indentation problems: a biography (1997–2000). Finite Elements Anal. Des. 37, 811–819.

Mackerle, J., 2002. Ceramics and ceramic matrix composites: finite element and boundary element analyses: a biography (1998–2000). Finite Elements Anal. Des. 38, 567–577.

Maw, N., Barber, J.R., Fawcett, J.N., 1976. The oblique impact of elastic spheres. Wear 38, 101–114.

Maw, N., Barber, J.R., Fawcett, J.N., 1981. The role of elastic tangential compliance in oblique impact. J. Lubr. Technol. ASME Transact. 103, 74–80.

Mecholsky, J., 2008. Private Communication. Department of Materials Science and Engineering, Univesity of Florida.

Mindlin, R.D., Deresiewicz, H., 1953. Elastic spheres in contact under varying oblique forces. J. Appl. Mech. 75, 327–344.

Miner, J.R., Dell, J., Galbato, A., Ragen, M.A., 1996. F-117-PW-100 hybrid bearing ceramic technology insertion. ASME J. Eng. Gas Turbines Power V 118, 434–442.

Ohgushi, K., Ichikawa, M., 1996. Fracture mechanics study of ring crack initiation in ceramics by sphere indentation. JSME Int. J. A Mech. Mater. Eng. 39 (4), 489–495.

Piotrowski, A.E., O'Brien, M.J., 2006. A novel test method to measure the fracture toughness of ceramic balls used in bearings. Fatigue Fract. Eng. Mater. Struct. 29, 558–572.

Sackfield, A., Hills, D.A., 1983. A note on the Hertz contact problem: a correlation of standard formulae. J Strain Anal. Eng. Des. 18 (2), 195–197.

Swenson, D., Ingraffea, A., 1987. A finite element model of dynamic crack propagation with an application to intersecting cracks. In: Proceedings of the Fourth International Conference on Numerical Methods in Fracture Mechanics. San Antonio, TX.

Swenson, D., Ingraffea, A., 1988a. Modeling mixed-mode dynamic crack propagation using finite elements: theory and applications. Comput. Mech. 3, 187–192.

Swenson, D., Ingraffea, A., 1988b. Using combined experiments and analysis to generate dynamic critical stress intensity data. In: Cruse, T. (Ed.), Fracture Mechanics: 19th Symposium. ASTM STP 969, Philadelphia, pp. 405–426.

Tanimoto, K., Kajihara, K., Yanai, K., 2000. Hybrid ceramic ball bearings for turbochargers, SAE Paper 2000-01-1339, pp. 1–14.
Wang, Y., Hadfield, M., 2000. The influence of ring crack location on the rolling contact fatigue failure of lubricated silicon nitride: experimental studies. Wear 243, 157–166.
Robert Wolfe, 2008. Private communication. Timken Co. (Research Sponsor).
Zhao, P., Hadfield, M., Wang, Y., Vieillard, C., 2006. Subsurface propagation of partial ring cracks under rolling contact. Part 1: Experimental studies. Wear 261, 382–389.